

pubs.acs.org/journal/apchd5 Article

A 3D-Printed Multicore Fiber-Tip Resonator for Ultrasonic Sensing

Baiqing Nan, Weijia Bao,* Zhihua Shao, Changrui Liao, Xuhui Sun, and Yiping Wang



Cite This: https://doi.org/10.1021/acsphotonics.5c01572

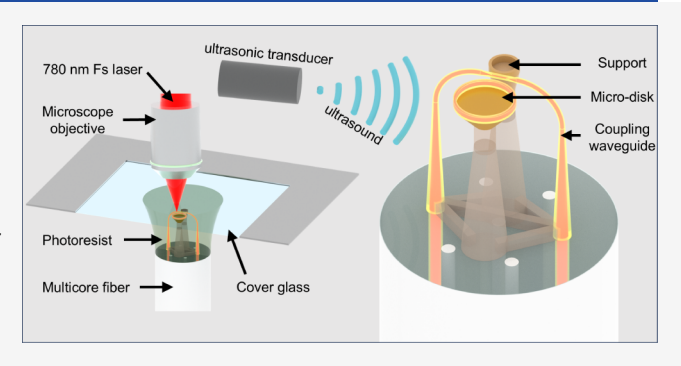


ACCESS

III Metrics & More

Article Recommendations

ABSTRACT: Optical fiber sensors have attracted considerable attention for ultrasonic detection, owing to their compactness and superior performance. In this study, leveraging two-photon polymerization technology in micronano fabrication, we have developed an ultrasonic sensor integrated with photonic wire bonding and an optical resonant microdisk, which are fabricated on the optical fiber end-face. The sensor demonstrates an ultrasonic sensitivity of 5.6 mV/kPa@1 MHz, a noise-equivalent pressure of 12.31 mPa/ $\sqrt{\text{Hz}@1}$ MHz, and the capability to detect ultrasonic signals over a 180° angular range. Furthermore, the sensor can be employed for the localization and imaging of small-scale objects. We perform a systematic experiment involving the linear translation



of the sensor to acquire ultrasonic signals, subsequently reconstructing the two-dimensional spatial profile of the fiber array. This fiber-tip ultrasonic sensor features compact dimensions, broad bandwidth, and elevated sensitivity, which demonstrate significant potential for diverse applications in ultrasonic wave-based sensing, imaging, and nondestructive testing.

KEYWORDS: two-photon 3D printing, whispering gallery mode, ultrasonic imaging, optical fiber sensor, 3D printing

■ INTRODUCTION

Ultrasonic sensors¹ and acoustic imaging technologies play a critical role in diverse applications, such as disease diagnosis,²,³ nondestructive testing,⁴,⁵ and industrial inspection.⁶⁻⁷ Piezoelectric transducers (PZTs) are currently the most widely utilized ultrasonic sensors.⁵,¹¹¹ However, with the advancement of ultrasonic detection technology and the increasing demand for applications across diverse fields, PZTs have progressively revealed certain limitations, including narrow bandwidth, large physical size, and susceptibility to electromagnetic interference.¹¹¹,¹¹² These shortcomings constrain their effectiveness in applications such as endoscopic imaging and large-area scanning imaging.¹³

In contrast, optical ultrasonic sensors effectively address the aforementioned challenges, 14 emerging as a focal point of research in the field of ultrasonic detection in recent years. 15,16 For example, Rong et al. develop a high-frequency 3D photoacoustic tomography system based on an on-chip microring resonator with a broadband ultrasonic response range of 23 MHz and noise equivalent pressure (NEP) as low as 81 Pa, enabling high-resolution imaging of biological tissues. Pan et al. demonstrate an on-chip microring sensor array based on a chalcogenide compound with an ultrasonic response bandwidth of 175 MHz and a NEP of 2.2 mPa/ $\sqrt{\text{Hz}}$ that can image fast-moving objects using a single light source and receiver. However, these on-chip optical resonators exhibit notable drawbacks, including significant challenges in device integration. Constrained by collimation and optical coupling

efficiency, the robustness of on-chip devices is comparatively low, which consequently limits their operational flexibility. As an alternative type of optical ultrasonic sensor, fiber-optic sensors eliminate the need for additional collimation and coupling processes, such as fiber Bragg gratings (FBGs)¹⁹ and Fabry-Perot interferometers (FPIs).²⁰ Beard et al. demonstrate a plano-concave polymer microresonator. This resonator achieves strong optical confinement resulting in very high sensitivity with excellent broadband ultrasonic frequency response and wide directivity. 21 Wen et al. fabricate an FPI ultrasonic sensor on the end face of an optical fiber through two-photon polymerization (TPP) 3D printing technology. The NEP reached 2.39 mPa/ $\sqrt{\mathrm{Hz}}$, enabling the detection of weak ultrasonic signals. 22 Similarly, Wei et al. utilized TPP 3D printing technology to fabricate a spring-shaped FPI on the fiber end face. By optimizing the operating frequency of the spring and sheet, they achieved an NEP of 2.39 mPa/ $\sqrt{\text{Hz.}^{23}}$ Nevertheless, fiberoptic sensors generally exhibit low Q-factors, resulting in reduced precision in ultrasonic measurements.

In this work, we propose and demonstrate a novel optical ultrasonic sensor that simultaneously achieves compact

Received: July 4, 2025
Revised: October 5, 2025
Accepted: October 6, 2025



dimensions, broad bandwidth, and elevated sensitivity. As shown in Figure 1, we utilize the end face of a seven-core fiber as

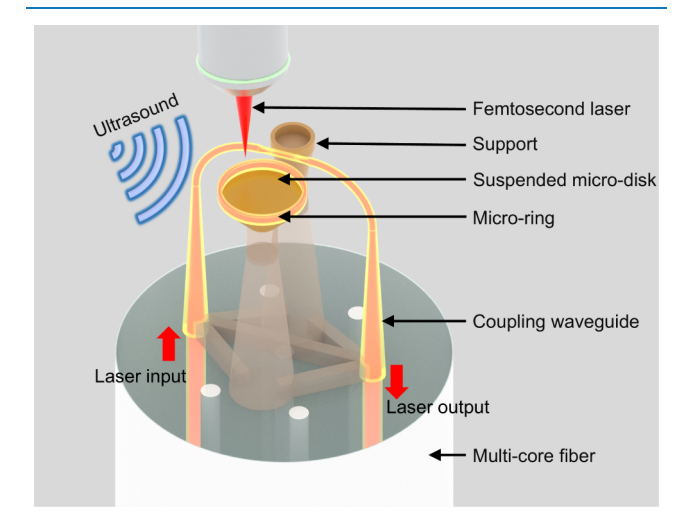


Figure 1. Schematic of the multicore fiber-tip resonator.

the processing substrate and fabricate sensing structures through TPP technology. First, we fabricate a photonic wire bond as coupling waveguides. Then, we fabricate two suspended microdisk structures, one of which serves as the waveguide support and the other as the ultrasonic sensitive element. By suspending the ultrathin microdisk structure above the substrate, it can efficiently detect mechanical vibrations induced by ultrasonic waves through the synergistic effect of mechanical and optical resonances. To enhance ultrasonic responsiveness, numerical optimization processes are employed to determine the optimal parameters, including diameter, width, and coupling distance. As a result of these optimizations, it exhibits a sensitivity of 5.6 mV/kPa at 1 MHz, a noise equivalent pressure of 12.31 mPa/ $\sqrt{\text{Hz}}$ at 1 MHz, and a sensing angle close to 180°. Finally, by performing ultrasound scanning with this sensor, we successfully achieve the imaging and localization of underwater targets.

PRINCIPLE AND SIMULATION

Figure 1 illustrates the structure of the fabricated fiber-optic ultrasonic sensor, which primarily comprises two key components: a coupling waveguide and suspended microdisks. We utilize a multicore fiber (MCF) as the processing substrate, wherein a coupling waveguide connects two cores of the MCF to achieve low-loss transmission. Light from the central region of the waveguide is coupled into the microdisk resonator, forming a Whispering Gallery Mode (WGM). This sensing configuration leverages the mechanical resonance of the microdisk and the optical resonance of the WGM to enable ultrasonic sensing. Therefore, prior to fabricating the structure, it is necessary to perform simulation and optimization of the parameters of these two key components to achieve great sensing performance.

Coupling Waveguide (Photonic Wire Bond, PWB). We investigated the parameters of the coupling waveguide. Previous reports had described a reflective prism structure integrated with a waveguide to connect the cores of a MCF.²⁴ However, this approach had significant optical loss and demanded high fabrication precision for the reflective surface to achieve total internal reflection. In this study, we adopted a low-loss optical coupling scheme that is employed in silicon photonic chips,

namely, photonic wire bonding (PWB).^{25–27} As depicted in Figure 2a, a U-shaped photonic wire bond connects two cores of

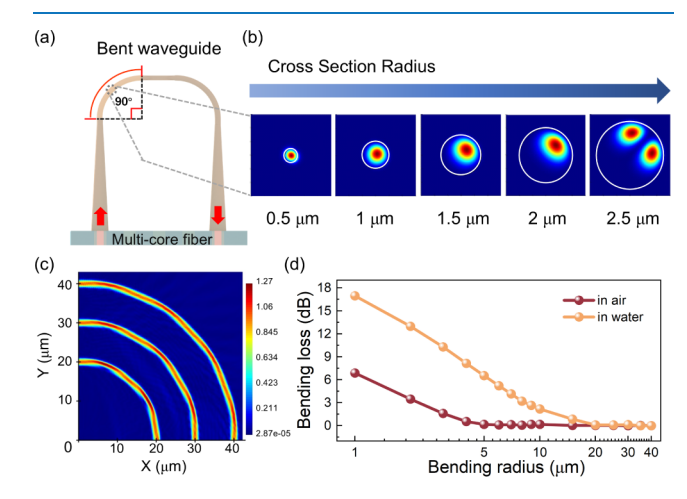


Figure 2. (a) U-shaped PWB. (b) Simulation of cross section mode analysis at 45° for bent waveguides with different cross section radiuses. (c) Simulation of optical transmission in waveguides with different bending radius. (d) Simulation results of bending loss corresponding to different bending radius (in water and air).

the MCF. To minimize connection loss, the input port is designed to be slightly larger than the fiber core. And, to facilitate lateral coupling and reduce bending loss, the waveguide adopts a tapered structure of which diameter of the PWB is reduced in the bending and coupling sections. The refractive index (RI) of PWB is 1.54, and the environmental RI is 1.0. Finite element analysis, as shown in Figure 2b, reveals that an increase in the diameter of the waveguide in the bending section leads to substantial mode mismatch loss due to bending. Moreover, at a diameter of 2.5 μ m, multimode excitation occurs. This phenomenon arises from bending-induced refractive index perturbation, which elevates the refractive index on the inner side of the waveguide, resulting in mode field deviation and energy leakage.

Additionally, the bending radius significantly influences light transmission. As demonstrated in Figure 2c,d, an increase in the bending radius markedly reduces bending loss. Notably, the reduced refractive index contrast requires a larger bending radius to achieve acceptable bending loss during transmission in water. A bending radius of 30 μ m is selected for the bending region because the sensor is intended for immersion in water during measurements. And, to ensure adequate mechanical strength of the waveguide, a diameter of 2 μ m was chosen for the coupling region. These parameters ensure optimal transmission performance for the PWB at the end-face of the MCF.

Optical Resonator. The resonant modes of the resonator cavity are analyzed in this section. If the light in the coupling waveguide satisfies the phase-matching condition, it will be confined within the resonator, forming a WGM. The free spectral range (FSR) of the WGM adheres to the following formula:

$$FSR = \frac{\lambda^2}{2n_{\text{eff}}\pi R} \tag{1}$$

where λ is the resonant wavelength, $n_{\rm eff}$ is the effective refractive index, and R is the radius of the resonator. It is evident that the resonant spectrum can be tuned by varying the diameter of the resonator. Importantly, as illustrated in Figure 1, we have

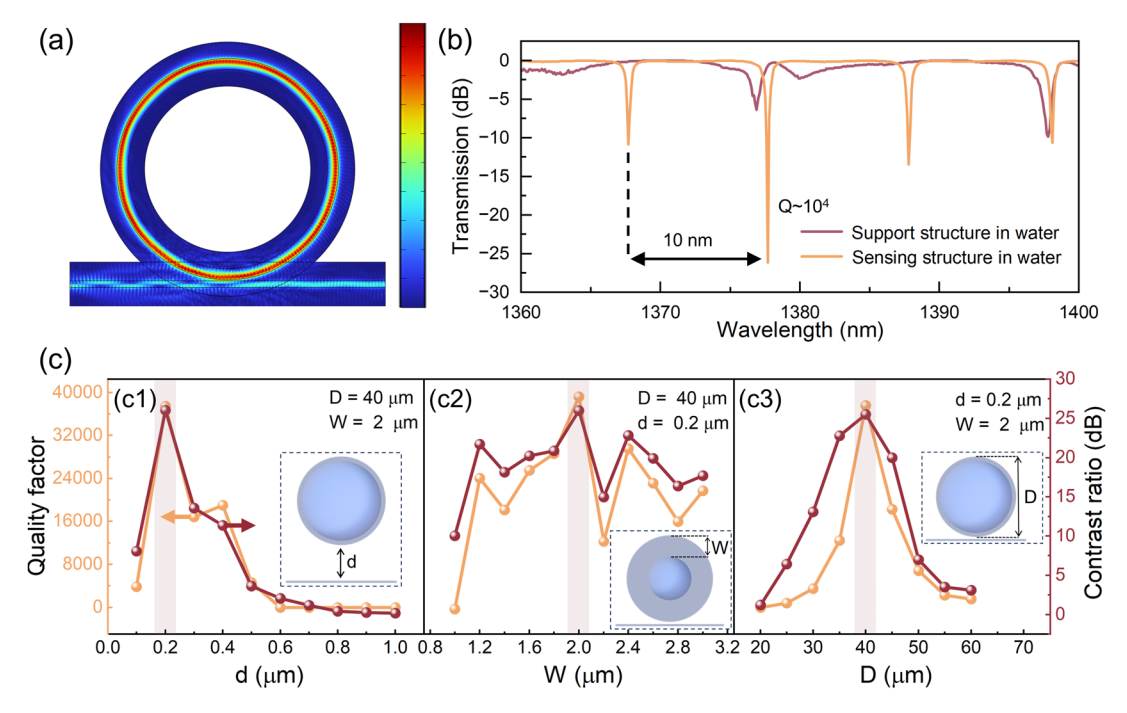


Figure 3. (a) Light profile of the resonator. (b) Simulation of the transmission spectrum of a microring in water. (c) Simulation of *Q*-factor and contrast of the microring in a water environment. c1: Simulation of different coupling distances. c2: Simulation of different widths. c3: Simulation of different outer diameters.

incorporated a microring structure on the boundary of the suspended microdisk to increase the coupling area, which can enhance the coupling efficiency between the waveguide and the resonator. Therefore, to optimize the coupling and thereby improve the Q-factor and spectral contrast of the resonator, we have utilized finite element analysis to establish the relationship between the resonant spectrum and the parameters of the microring. Figure 3a displays the simulated light profile of the microring at a resonant wavelength, demonstrating strong WGM coupling efficiency (simulation spectral range: 1360-1400 nm). Its transmission spectra in an aqueous environment are shown in Figure 3b. The resonance effect of the supporting structure is very weak, attributing to the overcoupling between the supporting structure and the coupling waveguide, as shown in Figure 6d. When the waveguide is extremely placed close to the resonant cavity, the coupling becomes excessively strong, causing light to couple into the cavity rapidly but also to escape quickly. Thereby this will effectively prevent coupling energy accumulation and further result in broadened line widths and shallower depths, making it difficult to observe resonance peaks in the spectrum. Consequently, the supporting structure designed in this work does not exert a significant influence on the resonance spectrum. Meanwhile, light propagates a certain distance within the support pillar, where the material inherently introduces optical losses. Larger microdisk dimensions exacerbate these losses. Therefore, to minimize such losses, we opted not to employ microdisks of identical size for support but instead designed smaller-sized microdisks for this purpose. Moreover, the sensing structure achieves a high Q factor of 10⁴ through simulation optimization in the following section. The optimized parameters include the coupling distance, ring width, and ring diameter, as depicted in Figure 3c1-c3. It can be observed that the trends of the Q-factor and the spectral contrast are generally consistent. The simulation results show that an excessively small coupling distance leads to overcoupling, while an excessively

large distance results in reduced coupling, see Figure 3c1. The optimal critical coupling distance is around 0.2 μ m. Moreover, as shown in Figure 3c2, the insufficient optical field confinement at smaller widths leads to a sharp increase in radiation loss, while the 2 μ m width achieves optimal field confinement with minimized radiation and surface scattering losses. In contrast, larger widths excite higher-order modes and expand the sidewall scattering area, inducing mode competition and additional losses. Furthermore, as shown in Figure 3c3, the smaller diameter and the insufficient bending radius of the microring lead to a sharp increase in bending loss and an increase in the proportion of surface scattering. The 40 μ m diameter balances the bending loss and scattering loss. The larger diameter and the increase in the optical path circumference cause the accumulation of surface scattering, and the influence of processing errors is magnified. Through global optimization in a multidimensional parameter space, the optimal structural configuration (d = 0.2 μ m, $W = 2 \mu$ m, $D = 40 \mu$ m) was determined, achieving a Q-factor exceeding 10⁴ and high transmission spectral contrast.

Mechanical Resonator. The mechanical resonance mechanism of the microdisk resonator is analyzed in this section. Mechanical resonance occurs when the frequency of an external periodic driving force matches the intrinsic frequency of the microdisk, resulting in significant periodic deformation. The mechanical optical resonance converts ultrasound-induced microdisk deformation into pronounced spectral shifts or intensity variations, enhancing sensitivity and frequency selectivity.

To simulate the response of a microdisk to ultrasound, the acoustic-structure interaction module in COMSOL was employed. The material properties were defined with a density (ρ) of 1200 kg/m³, Young's modulus (E) of 3×10^9 Pa, and Poisson's ratio (ν) of 0.32. The external environment was set to water, and the incident sound pressure was 10 Pa. The dimensions of the microdisk as an optical resonator were

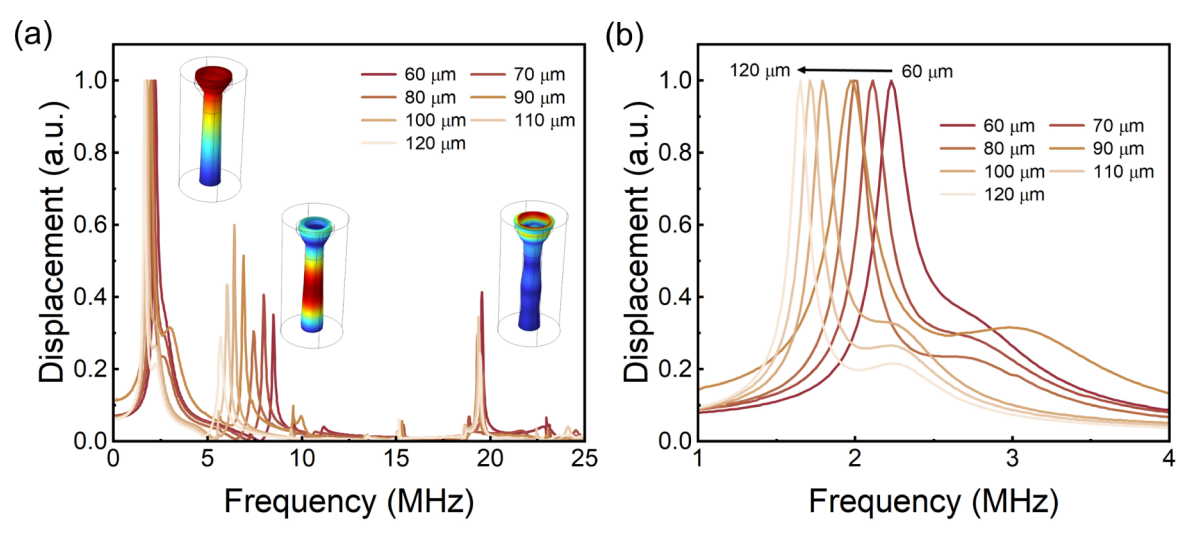


Figure 4. (a) Modal analysis of device resonance in water. (b) Simulation of first-order natural frequencies of the supporting structure with different heights.

established through prior optical simulations; these parameters were maintained consistently in the mechanical simulations. However, the support pillar, which serves to anchor the microdisk to the optical fiber, influences the overall mechanical resonance characteristics of the device. Accordingly, this section examines the impact of the support pillar height on the device's mechanical resonance properties. Figure 4a illustrates the sensor's resonance characteristics within the 0-25 MHz range, revealing three distinct resonance peaks, with the firstorder mode exhibiting the most pronounced amplitudefrequency response. Figure 4b depicts the variation in the firstorder resonance peaks, demonstrating a progressive decrease in the resonance frequency with increasing height. These results facilitate the selection of an appropriate frequency for the acoustic source transducer in subsequent acoustic measurements.

EXPERIMENT

Sensor Fabrication Method. Based on the aforementioned simulation parameters, the sensor was fabricated using TPP technology. The specific steps are as follows. First, the cleaved seven-core fiber (YOFC, MCF 7-42/150/250) was mounted on a custom-made holder to make its end face parallel to the cover glass. Then the knob on the holder was adjusted to bring the fiber close to the cover glass at a distance of 300 μ m, leaving enough space for printing the sensor model. The gap was filled with photoresist (IP-Dip, n = 1.54). Furthermore, the fiber is rotated to align the core with the coupled waveguide of the model, achieving the goal of efficient light transmission. The sensor model was sliced with a thickness of 200 nm both horizontally and vertically by software (DeScribe). Finally, control the three-dimensional micronano processing equipment (Nanoscribe GT) and use a 63× oil mirror (Carl Zeiss, NA = 1.4) to print out the model along the preset path. The femtosecond laser used a wavelength of 780 nm, a pulse width of 100 fs, and a repetition rate of 80 MHz. Under the optimization of the laser pulse energy (0.2 nJ) and scanning speed (50 mm/s), optimal fabrication fidelity was achieved. Following polymerization, remove the optical fiber and immerse it in propylene glycol monomethyl ether acetate (PGMEA) for approximately 20 s to dissolve uncured photoresist residues, thus completing the fabrication process. The printing effect is shown in Figures 5 and 6.

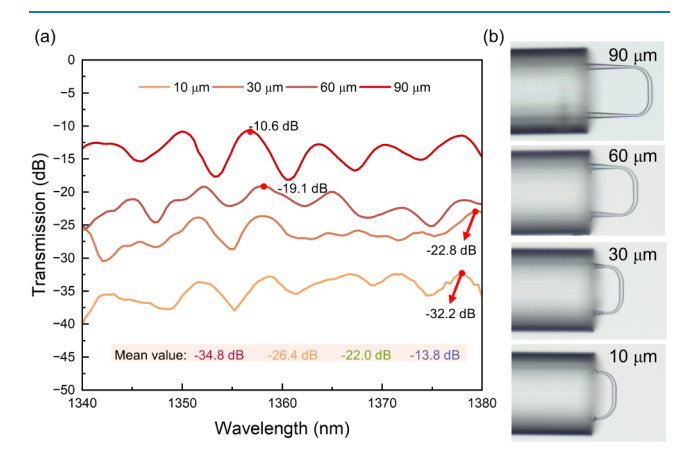


Figure 5. (a) Transmission spectrum of tapered waveguides with different lengths. The red dot represents the minimum loss value of tapered waveguides ranging from 1340 to 1380 nm. Mean loss is below the legend. (b) Microscopy images of tapered waveguides with lengths ranging from 90 to 10 μ m.

During the fabrication of the PWB waveguide, the waveguide must be sufficiently large at the fiber core coupling position to capture adequate optical flux, while it must be sufficiently thin to achieve effective coupling in the waveguide coupling region. Consequently, PWB should be printed as a tapered-gradient structure. However, the loss in a tapered waveguide is directly related to its taper angle. Abrupt changes will lead to significant losses. As shown in Figure 5, we reduced the taper angle of the waveguide by increasing its length, thereby effectively reducing the losses. When the wavelength was increased to 90 μ m, the mean loss decreased from approximately -34.8 dB to around −13.8 dB. Additionally, the coupling region of the PWB is prone to deformation and collapse due to its excessively thin diameter. To address this issue, we fabricated an additional supporting structure, as illustrated in Figure 6a-d. Since the supporting structure is in close proximity to the coupling region, the sensing spectrum would not be significantly affected due to the overcoupling. Figure 6a-d presents scanning electron micro-

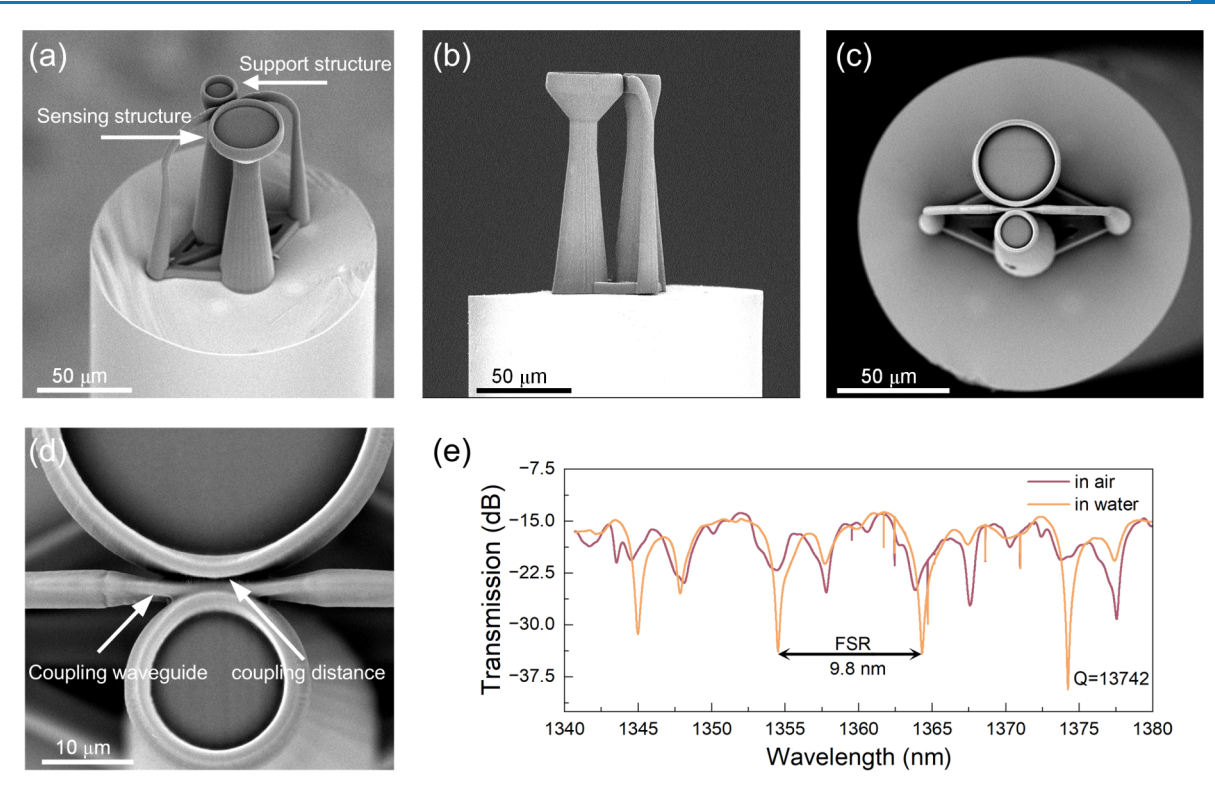


Figure 6. (a) Strabismus view of the sensor. (b) Side view of the sensor. (c, d) Top view and details of the sensor. (e) Transmission spectra in air and water.

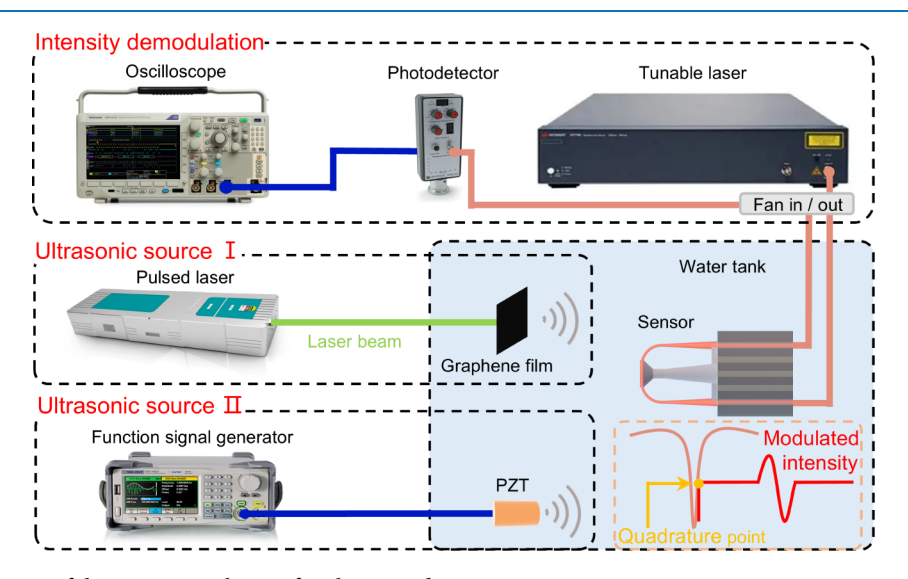


Figure 7. Schematic diagram of the experimental setup for ultrasonic detection.

scope (SEM) images of the fabricated device. Figure 6e shows the transmission spectrum of the sensor with an FSR of 9.8 nm, which is in good agreement with the previous simulation analysis. Upon immersing the sensor in water, the spectrum was improved, and the *Q*-factor is 13 742. This improvement is attributed to water acting as a cladding layer, which enhances the optical transmission capability of the PWB.²⁸

Ultrasonic Performance Detection. This sensing configuration leverages the mechanical resonance of the microdisk and the optical resonance of the WGM to enable ultrasonic sensing. The fabricated fiber-optic end-face resonator can effectively detect ultrasonic waves. The experimental setup for ultrasonic detection is illustrated in Figure 7, wherein the sensor is

immersed in a water tank. Light from a tunable laser (Keysight N7778C) was directed into a fan-in/fan-out device and subsequently was input into the sensor. The output light from the sensor was then transmitted to a photodetector (PD, New Focus 2053), which converted the optical signal to an electrical signal for analysis by an oscilloscope. In this study, we employed intensity demodulation based on sideband filtering. The wavelength of the tunable laser was precisely locked onto the sideband of the sensor's resonance peak.

To characterize the sensor's response bandwidth, broadband ultrasound generated by irradiating a graphene film with a nanosecond laser was utilized as the source. The sensor's timedomain and frequency-domain responses are presented in

Figure 8a,b. The sensor exhibits multiple resonance peaks across a wide frequency band, demonstrating its capability for ultrasonic detection over various frequency ranges.

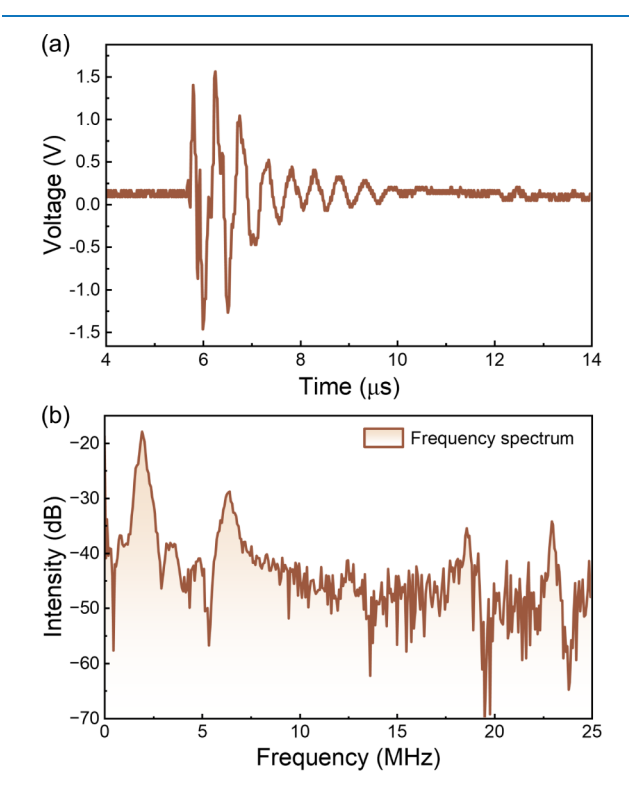


Figure 8. (a) Time-domain signal detected by an ultrasonic sensor. (b) Frequency-domain response.

Further, to evaluate the sensor's ultrasonic response capability, a water-immersed piezoelectric transducer (PZT, Olympus A303S) with a resonance frequency of 1 MHz driven by a signal generator was employed as the source. The sensor was positioned 2 cm in front of the PZT, and ultrasound was initially triggered by using a pulsed method. As depicted in Figure 9a, the sensor's response exhibits a peak-to-peak voltage of 249.35 mV, with a root-mean-square (RMS) noise voltage of 0.88 mV. Through fast Fourier transform (FFT), the amplitude-frequency characteristic of the sensor was determined to be 1.09 MHz, as shown in Figure 9b, thereby confirming its responsiveness to ultrasound. The signal-to-noise ratio (SNR) can be calculated by using the formula:

$$SNR = 20 \times \log_{10} \frac{\nu_1}{\nu_2} \tag{2}$$

where v_1 is the peak-to-peak voltage of the pulse signal and v_2 is the RMS of the noise voltage. This indicates that the sensor has a high SNR of 49 dB. Noise equivalent pressure (NEP) can be calculated by the following formula:²²

$$NEP = \frac{p \times 10^{\frac{-SNR}{20}}}{\sqrt{\Delta f}}$$
 (3)

where p is the sound pressure at the sensor and Δf is the measurement bandwidth. According to the calibration result of the hydrophone, the sound pressure received by the sensor is 15.52 kPa. The NEP is calculated to be 12.31 mPa/ $\sqrt{\text{Hz}}$.

Subsequently, ultrasound was triggered using a sinusoidal voltage, with the sensor's response illustrated in Figure 9c. The

sensor demonstrated a robust sinusoidal response, achieving a sensitivity of up to 5.6 mV/kPa, see Figure 9d. Additionally, the frequency spectrum remained accurately centered at 1 MHz, see Figure 9e. Moreover, the amplitude of the detected signals versus the measuring angle is shown in Figure 9f, where the inset shows the testing setup. The primary acoustic sensing mechanism of the sensor relies on the modulation of the microdisk's refractive index induced by incident acoustic waves. Experimental results reveal that, irrespective of the propagation direction of the acoustic wave toward the sensor, it couples into the microdisk, thereby altering its refractive index. Consequently, the sensor demonstrated a very broad angular response.

Ultrasonic Imaging. Based on its excellent ultrasonic response, the ultrasonic sensor was subsequently deployed in ultrasound imaging experiments to demonstrate its objectresolving capabilities. The principle of the experimental process is shown in Figure 10a. The target object for ultrasonic imaging consists of three fibers with diameters of 550, 400, and 250 μ m, respectively. The sensor is held by an optical fiber clamp and controlled by a two-axis translation stage, moving from right to left at equal intervals of 20 μ m. Ultrasonic waves generated by a 5 MHz PZT (PZT, Olympus V326-SU) were reflected off the surfaces of the fibers and subsequently detected by the sensor. Figure 10b shows the actual device diagram in water. Figure 10c clearly demonstrates the working principle of the delay and sum (DAS) image reconstruction algorithm: calculating the time from each piezoelectric ion to each sensor, delaying the signal received by the sensor unit, aligning it in the time domain, and then superimposing the delay signal, which can enhance the ultrasonic signal in a specific direction to suppress the noise. Figure 10d shows the processing of ultrasonic signals, and in Figure 10d1 the noise on the far left is introduced by PZT. Therefore, in the process of signal processing, noise and ultrasonic signal are first distinguished, the noise signal is removed, and then the SNR of the ultrasonic signal is improved by filtering, transforming, taking the envelope, and other methods, as shown in Figure 10d2,d3. Then the image is reconstructed using the DAS algorithm, and the spatial distribution of the image is consistent with the actual situation. Color conversion or log compression will be used to make the image better. Finally, an ultrasonic image is obtained, as shown in Figure 10d4. The three yellow dots distributed from the top left to the bottom right of the figure correspond to three fibers. As the imaging depth increased, the reflected ultrasonic signal attenuated significantly, resulting in weaker imaging performance for the 250 μm diameter fiber. Based on the results, the sensor is capable of reconstructing the positions and cross sections of these three fibers.

CONCLUSION

In this work, we integrated a WGM optical microcavity with an optical fiber to develop a novel ultrasonic sensor. The sensor was fabricated using two-photon polymerization 3D printing technology, and its ultrasonic detection performance was thoroughly characterized. By performing a comparative analysis of various microdisk structural parameters, we identified the optimal design. The sensitivity reached 5.6 mV/kPa at 1 MHz, with an NEP of 12.31 mPa/ $\sqrt{\rm Hz}$ at 1 MHz. This system successfully enabled the precise localization of underwater objects and the high-resolution imaging of small objects. The proposed design of the novel ultrasonic sensor provides valuable insights and holds significant potential for applications in the

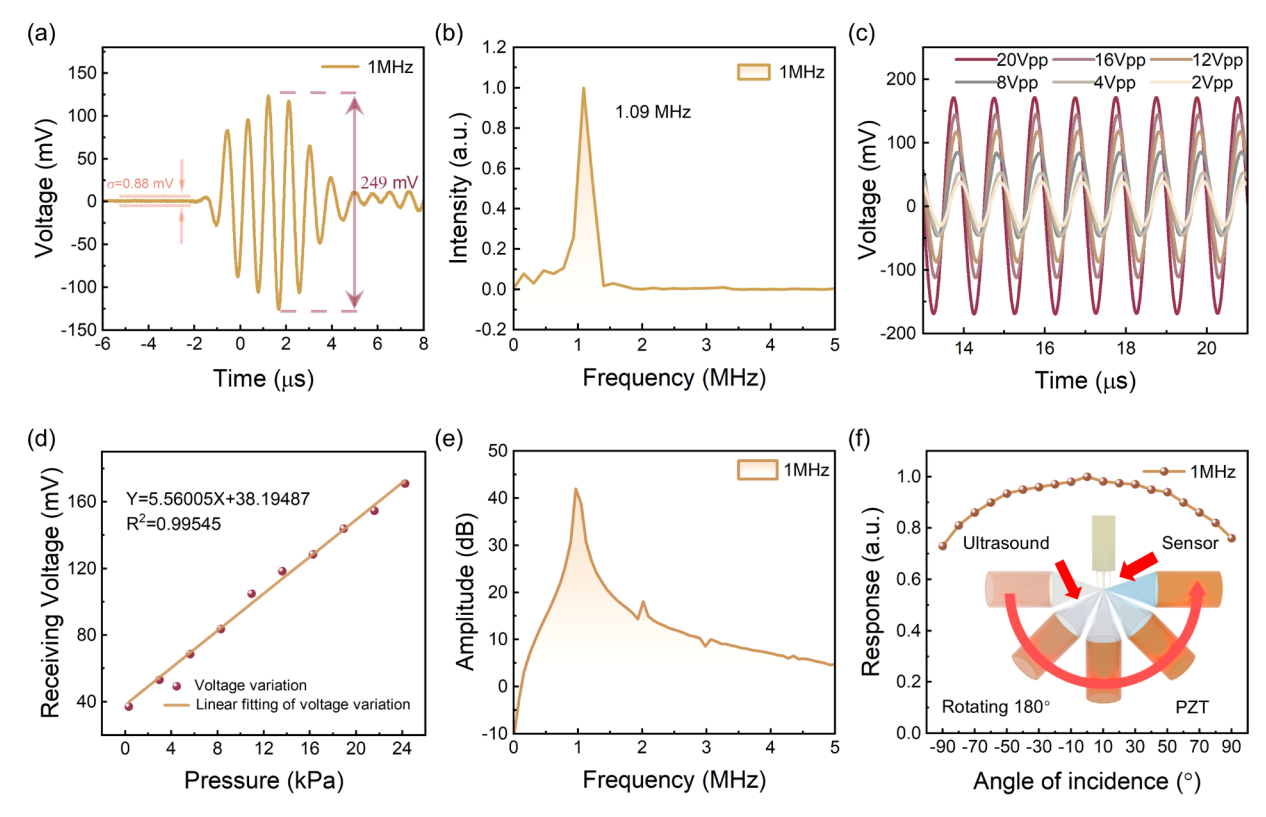


Figure 9. (a) Pulse signal response. (b) FFT of the pulse signal. (c) Time signal collected by the sensor at different voltages at a frequency of 1 MHz. (d) The voltage sensitivity of the sensor. (e) FFT of the sinusoidal time domain signal when the PZT drive voltage is 20 Vpp. (f) The normalized angular response of the sensor. Inset: Angular response diagram.

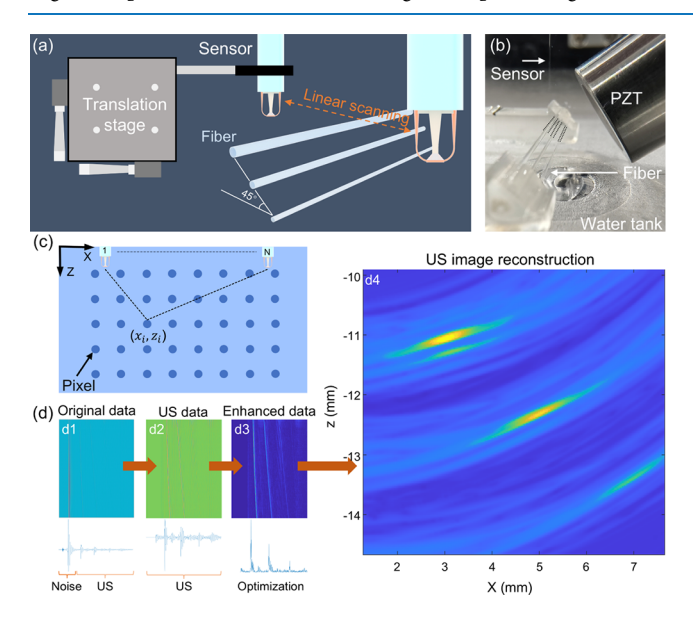


Figure 10. (a) Schematic of the experimental principle. (b) Actual device diagram. (c) Das algorithm. (d) Image reconstruction process. d1: Raw signal with PZT introduced noise. d2: Signal after splitting noise. d3: Signal after processing. d4: Image reconstruction.

field of photoacoustic imaging, industrial nondestructive testing, and other fields.

AUTHOR INFORMATION

Corresponding Author

Weijia Bao – Guangdong and Hong Kong Joint Research Centre for Optical Fibre Sensors, Shenzhen University, Shenzhen 518060, China; Shenzhen Key Laboratory of Ultrafast Laser micro/Nano Manufacturing, Shenzhen University, Shenzhen 518060, China; orcid.org/0009-0008-8598-3056; Email: wjbao@szu.edu.cn

Authors

Baiqing Nan — Guangdong and Hong Kong Joint Research Centre for Optical Fibre Sensors, Shenzhen University, Shenzhen 518060, China; Shenzhen Key Laboratory of Ultrafast Laser micro/Nano Manufacturing, Shenzhen University, Shenzhen 518060, China

Zhihua Shao — School of Physics, Northwest University, Xi'an 710069, China

Changrui Liao — Guangdong and Hong Kong Joint Research Centre for Optical Fibre Sensors, Shenzhen University, Shenzhen 518060, China; Shenzhen Key Laboratory of Ultrafast Laser micro/Nano Manufacturing, Shenzhen University, Shenzhen 518060, China; orcid.org/0000-0003-3669-5054

Xuhui Sun — Guangdong and Hong Kong Joint Research Centre for Optical Fibre Sensors, Shenzhen University, Shenzhen 518060, China; Shenzhen Key Laboratory of Ultrafast Laser micro/Nano Manufacturing, Shenzhen University, Shenzhen 518060, China

Yiping Wang — Guangdong and Hong Kong Joint Research Centre for Optical Fibre Sensors, Shenzhen University, Shenzhen 518060, China; Shenzhen Key Laboratory of Ultrafast Laser micro/Nano Manufacturing, Shenzhen University, Shenzhen 518060, China

Complete contact information is available at: https://pubs.acs.org/10.1021/acsphotonics.5c01572

Author Contributions

B.N.: Conceptualization, data curation, formal analysis, investigation, methodology, validation, visualization, and writing (Original draft). W.B.: Formal analysis, funding acquisition, investigation, methodology, project administration, supervision, and writing (review and editing). Z.S.: Conceptualization and writing (review and editing). X.S.: Investigation and methodology. C.L.: Conceptualization and writing (review and editing). Y.W.: Conceptualization, funding acquisition, supervision, and writing (review and editing).

Funding

This work was supported by the National Key Research and Development Program of China (2023YFB3209500), Shenzhen Science and Technology Program (JCYJ20241202124226032, JCYJ20220818095800001, Shenzhen Key Laboratory of Ultrafast Laser Micro/Nano Manufacturing ZDSYS20220606100405013), and Special Fund for the Cultivation of Independent Innovation Achievements of Postgraduate Students at Shenzhen University (000066010716).

Notes

The authors declare no competing financial interest.

REFERENCES

- (1) Yang, L.; Li, Y.; Fang, F.; Li, L.; Yan, Z.; Zhang, L.; Sun, Q. Highly sensitive and miniature microfiber-based ultrasound sensor for photoacoustic tomography. *Opto-Electron. Adv.* **2022**, *5*, 200076.
- (2) Kou, S.; Thakur, S.; Eltahir, A.; Nie, H.; Zhang, Y.; Song, A.; Hunt, S. R.; Mutch, M. G.; Chapman, W. C.; Zhu, Q. A portable photoacoustic microscopy and ultrasound system for rectal cancer imaging. *Photoacoustics* **2024**, *39*, 100640.
- (3) Liu, X.; Li, H.; Pang, M.; Liu, J.; Song, X.; He, R.; He, M.; Jian, X.; Ma, C.; Deng, H.; et al. Photoacoustic imaging in brain disorders: Current progress and clinical applications. *VIEW* **2024**, *5* (4), 20240023.
- (4) Teng, F.; Wei, J.; Lv, S.; Geng, X.; Peng, C.; Zhang, L.; Jia, L.; Jiang, M. Damage localization in carbon fiber composite plate combining ultrasonic guided wave instantaneous energy characteristics and probabilistic imaging method. *Measurement* **2023**, 221, 113443.
- (5) Chai, Y.; Wu, Q.; Yan, J.; Liu, Q.; Qing, X. Failure monitoring and localization of wind turbine blades using ultrasonic guided waves and multi-index fusion imaging. *Eng. Fail. Anal.* **2025**, *170*, 109326.
- (6) Xie, L.; Lian, Y.; Du, F.; Wang, Y.; Lu, Z. Optical methods of laser ultrasonic testing technology in the industrial and engineering applications: A review. *Opt. Laser Technol.* **2024**, *176*, 110876.
- (7) Wang, Y.; Zhang, W.; Chen, D.; Zhang, G.; Gong, T.; Liang, Z.; Yin, A.; Zhang, Y.; Ding, W. Defects detection in metallic additive manufactured structures utilizing multi-modal laser ultrasonic imaging integrated with an improved MobileViT network. *Opt. Laser Technol.* 2025, 187, 112802.
- (8) Zhang, K.; Yan, B.; Li, H.; Lin, J.; Wu, J.; Yan, Z.; Sun, Q. High-Precision Flow Rate Measurement Based on Distributed Optical Fiber Acoustic Sensing. *Photonic Sens.* **2025**, *15* (3), 250313.
- (9) Deng, H.; Bai, Y.; Xiang, J.; Li, Z.; Zhao, P.; Shi, Y.; Fu, W.; Chen, Y.; Fu, M.; Ma, C.; Luo, B. Photoacoustic/ultrasound dual-modality imaging for marker clip localization in neoadjuvant chemotherapy of breast cancer. *J. Biomed. Opt.* **2024**, *29*, S11525.
- (10) Tanveer, M.; Elahi, M. U.; Jung, J.; Azad, M. M.; Khalid, S.; Kim, H. S. Recent Advancements in Guided Ultrasonic Waves for Structural Health Monitoring of Composite Structures. *Appl. Sci.* **2024**, *14*, 11091.
- (11) Suzuki, M.; Tagawa, N.; Yoshizawa, M.; Irie, T. Effects of flexural vibration and thickness vibration on receiving characteristics of a diaphragm-type PZT resonator. *Jpn. J. Appl. Phys.* **2020**, *59*, SKKE10.
- (12) Schneider, M.; Dorfmeister, M.; Moll, P.; Kaltenbacher, M.; Schmid, U. Bi-Stable Aluminum Nitride-Based Piezoelectric Micro-

- machined Ultrasonic Transducer (PMUT). J. Microelectromech. 2020, 29, 948–953.
- (13) Li, X.; Stritch, T.; Manley, K.; Lucas, M. Limits and Opportunities for Miniaturizing Ultrasonic Surgical Devices Based on a Langevin Transducer. *IEEE Trans. Ultrason. Ferroelectr. Freq. Control* **2021**, *68*, 2543–2553.
- (14) Wang, A.; Fan, X.; Chen, G.; Liu, Y.; Li, Z.; Zhang, Z.; Wang, X.; Zhang, F.; Zhang, Z.; Qiu, H.; Gao, H.; Xiong, W.; Li, H.; Sun, Q. Ultrahigh-Sensitivity 3D-Printed Hollow Fabry-Perot Fiber-Ultrasound Sensor for Photoacoustic Imaging. *ACS Photonics* **2025**, *12*, 4553–4562.
- (15) Cao, X.; Yang, H.; Wu, Z.-L.; Li, B.-B. Ultrasound sensing with optical microcavities. *Light: Sci. Appl.* **2024**, *13* (1), 159.
- (16) Sun, J.; Tang, S.-J.; Meng, J.-W.; Li, C. Whispering-gallery optical microprobe for photoacoustic imaging. *Photonics Res.* **2023**, *11*, A65.
- (17) Rong, Q.; Lee, Y.; Tang, Y.; Vu, T.; Taboada, C.; Zheng, W.; Xia, J.; Czaplewski, D. A.; Zhang, H. F.; Sun, C.; et al. High-Frequency 3D Photoacoustic Computed Tomography Using an Optical Microring Resonator. *BME Front.* **2022**, 2022, 9891510.
- (18) Pan, J.; Li, Q.; Feng, Y.; Zhong, R.; Fu, Z.; Yang, S.; Sun, W.; Zhang, B.; Sui, Q.; Chen, J.; et al. Parallel interrogation of the chalcogenide-based micro-ring sensor array for photoacoustic tomography. *Nat. Commun.* **2023**, *14*, 3250.
- (19) Choi, S.; Kim, J.; Jeon, H.; Kim, C.; Park, E.-Y. Advancements in photoacoustic detection techniques for biomedical imaging. *Npj Acoust.* **2025**, *1*, 1.
- (20) Li, L.; Fan, X.; Chen, G.; Liu, Y.; Zhang, F.; Chen, Z.; Zhang, Z.; Xu, W.; Zhang, S.; Liu, Y.; et al. From fish to fiber: 3D-nanoprinted optical neuromast for multi-integrated underwater detection. *Nat. Commun.* **2025**, *16*, 7390.
- (21) Guggenheim, J.; Li, J.; Allen, T.; Colchester, R.; Noimark, S.; Ogunlade, O.; Parkin, I.; Papakonstantinou, I.; Desjardins, A.; Zhang, E.; Beard, P. Ultrasensitive plano-concave optical microresonators for ultrasound sensing. *Nat. Photonics* **2017**, *11*, 714–719.
- (22) Wen, J.; Yang, T.; Zheng, Z.; Xi, T.; Liu, Z.; Wei, H. Two-Photon 3D-Printed Fabry-Pérot Interferometric Sensor for Ultrasensitive High-Frequency Ultrasonic Detection. *J. Lightwave Technol.* **2025**, 43, 948–956.
- (23) Wei, H.; Wu, Z.; Sun, K.; Zhang, H.; Wang, C.; Wang, K.; Yang, T.; Pang, F.; Zhang, X.; Wang, T.; Krishnaswamy, S. Two-photon 3D printed spring-based Fabry—Pérot cavity resonator for acoustic wave detection and imaging. *Photonics Res.* **2023**, *11*, 780–786.
- (24) Sun, J.; Hou, F.; Feng, S.; Li, C. Integrated Optical Microrings on Fiber Facet for Broadband Ultrasound Detection. *Adv. Sens. Res.* **2024**, 3 (12), 2400076.
- (25) Billah, M. R.; Blaicher, M.; Hoose, T.; Dietrich, P.-I.; Marin-Palomo, P.; Lindenmann, N.; Nesic, A.; Hofmann, A.; Troppenz, U.; Moehrle, M.; Randel, S.; Freude, W.; Koos, C. Hybrid integration of silicon photonics circuits and InP lasers by photonic wire bonding. *Optica* **2018**, *5*, 876–883.
- (26) Rhee, H. W.; Shim, J.; Kim, J. Y.; Bang, D. J.; Yoon, H.; Kim, M.; Kim, C. C.; You, J. B.; Park, H. H. Direct optical wire bonding through open-to-air polymerization for silicon photonic chips. *Opt. Lett.* **2022**, 47, 714–717.
- (27) Practical Applications of Microresonators in Optics and Photonics; Matsko, A. B. Eds.; CRC Press, 2018; Vol. 3, p. 586. DOI: .
- (28) Melloni, A.; Costa, R.; Cusmai, G.; Morichetti, F. The role of index contrast in dielectric optical waveguides. *Int. J. Mater. Prod. Technol.* **2009**, 34, 421–437.